npj | materials degradation

Article

Published in partnership with CSCP and USTB

https://doi.org/10.1038/s41529-024-00494-2

Mechanistic investigation on the influence of coating weights on the corrosion behaviour of hot-dip-galvanised Zn-Mg-Al coatings

A. D. Malla[1] ✉, J. H. Sullivan[1], D. J. Penney[1], M. Goldsworthy[1], D. Britton[1], G. Williams[1], F. Goodwin[2] & A. P. Cardoso[3]

Time-lapse Microscopy, scanning vibrating electrode technique and potentiodynamic methods were used to study the influence of increasing coating weight (80–310 gm^{-2}) on microstructure, cut-edge and surface corrosion of Zn-Mg-Al coatings in 0.17 M NaCl. Cut-edge corrosion was similar for all coatings due to the oxygen reduction reaction becoming diffusion-limited. A 64% reduction in surface corrosion was observed for high coating weights through increases in eutectic volume fraction. Spatial and temporal corrosion mechanisms were controlled by microstructural morphological differences as coating weight varied. 80 $g.m^{-2}$ coatings demonstrated lateral anodic spreading potentially reducing coating penetration rates despite their higher surface corrosion rate.

For decades, researchers have been developing surface treatments to prevent steel from corroding to extend its service life. Among the surface treatments, the application of zinc (Zn) to a steel substrate via hot-dip galvanising (HDG) has been accepted and used in various industries since the 1800s[1]. Batch galvanising is normally used for bulk and geometrically complex products whereas continuous galvanising is more suitable for coiled products i.e., wire and sheet. Zn coatings protect underlying steel by two methods: barrier and galvanic protection. In barrier protection, the Zn coating isolates the steel from the corrosive environment while in galvanic protection, Zn being more anodic to the steel will sacrificially protect the steel substrate. Furthermore, additional protection is provided from the precipitation of corrosion products[2]. Efforts to improve and optimise the corrosion resistance of HDG Zn coatings have focused on alloying with aluminium (Al), magnesium (Mg) or both[3]. This enables the lower coating thickness to be employed without a reduction in corrosion performance. A HDG Zn bath contains low levels of Al (<0.20%) to reduce zinc oxidation, improve the lustre of the coating and prevent the formation of coarse iron (Fe) / zinc intermetallics[1,4,5]. Steel with standard HDG coating corrodes 10–20 times slower than bare steel substrate[6]. Binary Zinc-Aluminium (Zn-Al) metallic coatings containing 5 wt.%–55 wt.% Al exhibited much higher corrosion resistance than standard HDG coating due to the formation of Al-based corrosion products[7,8].

In the last decade, Zinc (Zn) - Magnesium (Mg) – Aluminium (Al) (Zn-Mg-Al also known as ZMA) alloy coatings with Mg and Al wt. % levels <5 wt. % have received significant interest in the scientific literature and with manufacturers. Studies have demonstrated that ZMA coatings provide improved resistance to corrosion compared to HDG Zn and Zn-Al coatings in a range of electrolytes, particularly in the presence of chloride ions[9–12]. This enhancement in corrosion resistance is attributed to the unique microstructure and the formation of stable corrosion products absent on HDG Zn and Zn-Al coatings[13–15]. Industrially produced ZMA coatings generally have microstructures composed of Zn dendrites, a Mg-rich binary eutectic phase and an Al-containing ternary eutectic phase[16]. It has been demonstrated that the ZMA corrosion mechanism is highly localised and corrodes via the anodic dissolution of Mg from $MgZn_2$ present in the binary eutectic phase[17,18]. The formation of $Mg(OH)_2$ due to Mg^{2+} release suppresses the cathodic oxygen reduction reaction[17,19]. In addition, a favourable electrochemical environment is created in which Zn surfaces passivate[15,20] and anodic activation of Al phases occurs that react with Mg^{2+} to produce protective double-layered hydroxide[15,21]. As the corrosion mechanism of ZMA is highly localised the extent of localisation could vary with the change in microstructure[17]. Processing parameters such as cooling rate and coating thickness can considerably modify the microstructure of the same composition coating. Previously, an investigation on the influence of the coating thickness of Zn – 5 wt.% Al revealed quantifiable differences in microstructural phase size, volume fraction and distribution[22]. Thus far limited investigations have been conducted to study the effects of process conditions. Investigations on the influence of cooling rate on surface corrosion[21,23]

[1]Corrosion and Coatings Group, Department of Materials, Swansea University, Bay Campus, Fabian Way, Crymlyn Burrow, Swansea, SA1 8EN, UK. [2]International Zinc Association, Durham, NC, 27713, USA. [3]International Zinc Association, Brussels, 1150, Belgium. ✉e-mail: amar.malla@swansea.ac.uk

and coating thickness on filiform corrosion[24] of ZMA coatings have been conducted. However, limited published studies have been conducted to investigate the influence of coating thickness (coating weights) on the cut-edge and surface corrosion of ZMA coatings. Thus, further systematic investigations need to be performed on ZMA coatings to assess changes in corrosion behaviour that come about as a result of microstructural changes induced by variations in coating thickness (coating weight).

This mechanistic study provides insights into the localised corrosion behaviour and corrosion performance due to changes in the thickness of ZMA coatings. The effect of coating thickness in terms of microstructural changes and its subsequent corrosion behaviours in 0.17 M NaCl is investigated using a range of techniques. The corrosion of ZMA coatings immersed in 0.17 M NaCl has been previously investigated using Time-lapse Microscopy (TLM) and Scanning Vibrating Electrode Technique (SVET)[17,21] therefore using 0.17 M NaCl in this investigation will enable us to examine the subtle changes in corrosion activities. TLM and SVET were utilized to understand the localised corrosion mechanism and evaluate the corrosion performance. The investigation was complemented by open circuit potential (OCP) and linear polarisation resistance (LPR) measurements.

Results

Materials characterisation

The ZMA coatings with various coating weights, alongside the coating thickness, applied to a 1.2 mm steel sheet used in this investigation are presented in Table 1. Coating weights of 80 $g.m^{-2}$, 200 $g.m^{-2}$ and 310 $g.m^{-2}$ were investigated. The coating thickness was measured using cut-edge SEM images. The errors shown are based on the standard deviation of ten measurements.

Table 1 | ZMA samples with various coating weights under investigation

Sample	Coating weight ($g.m^{-2}$)	Coating thickness per side (μm)
ZMA80	80	6.95 ± 1.06
ZMA200	200	13.31 ± 1.52
ZMA310	310	27.12 ± 1.59

The microstructure of ZMA is composed of a Zn dendritic phase and two eutectic phases; binary eutectic and ternary eutectic[17]. Binary eutectics consisted of Zn and intermetallic $MgZn_2$ whilst ternary eutectics consisted of Zn, $MgZn_2$ and Al nodules. The microstructures of different coating weights samples (ZMA80, ZMA200 and ZMA310) are shown in Fig. 1. Figure 1A–C shows the surface microstructure whereas Fig. 1D–F shows the through-coating microstructure.

The increase in coating thickness with an increase in coating weight can also be observed in Fig. 1D–F. For the lowest coating weight (ZMA80) a very fine microstructure was observed with the primary Zn phase having a globular morphology. For the higher coating weights (ZMA200 and ZMA310), coarser microstructures with larger Zn dendrites were observed. The volume fraction of the Zn phase and eutectic phase varied as the coating weight increased from 80 $g.m^{-2}$ to 200 $g.m^{-2}$ and 310 $g.m^{-2}$ as shown in Table 2. The errors are based on the standard deviation of five measurements. ZMA200 and ZMA310 demonstrate similar volume fractions for both Zn and eutectic phases. However, there is a decrease in the Zn phase volume fraction from 84.03% in ZMA80 to 65.19% in ZMA200 and 70.87% in ZMA310. Whereas the eutectic phase increased from 15.97% for ZMA80 to 34.81% for ZMA200 and 29.13% for ZMA310.

The average primary Zn size, the surface area fraction of Zn and the eutectic phases were determined by analysing the circular area of 0.78 mm^2 exposed to electrolyte during the TLM experiments are shown in Table 3. These measurements were made so that the influence of the exact surface microstructure exposed to the electrolyte could be assessed with regard to the corrosion behaviour. The average area of individual zinc dendrite size increased with coating weights and was 115 μm^2, 353 μm^2 and 363 μm^2 for ZMA80, ZMA200 and ZMA310, respectively. Analogous to volume fraction (Table 2), ZMA200 and ZMA310 demonstrate similar area fractions for both Zn and eutectic phases whereas the ZMA80 had a larger surface area of Zn with reduced eutectic levels. The area fraction of Zn phases decreased from 70.1% for ZMA80 to 50% for ZMA310. Consequently, the area fraction of the eutectic phase increased from 29.9% for ZMA80 to 50% for ZMA310.

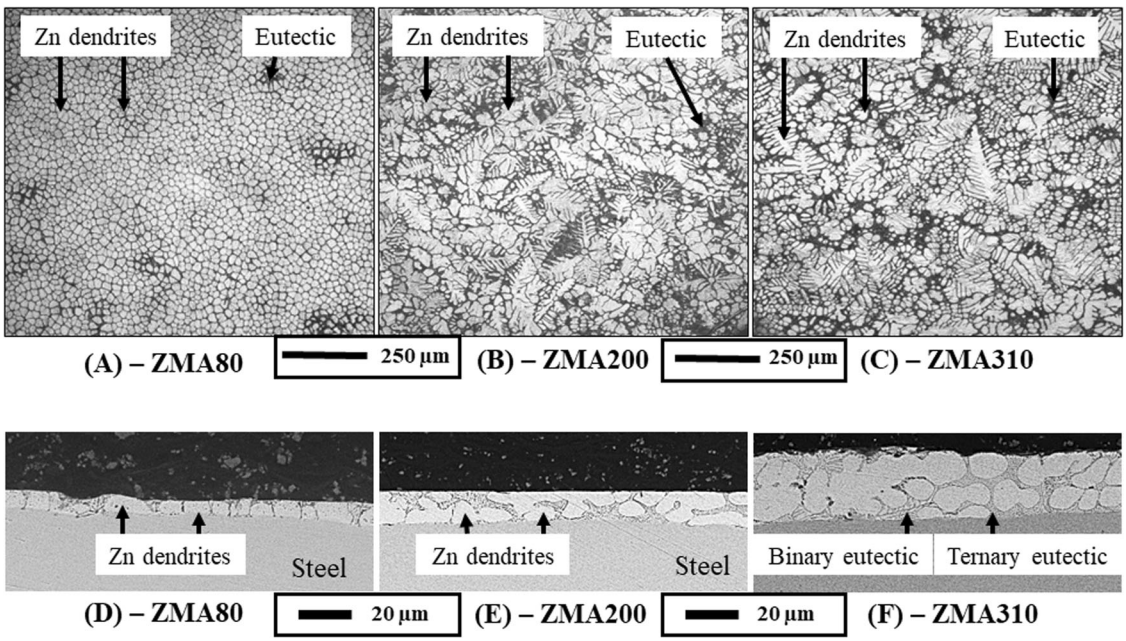

Fig. 1 | SEM images showing the microstructures of different coating weights ZMA samples. A–C shows surface microstructure and **D–F** shows the cut-edge microstructure. The microstructure is transformed from finer to coarser with an increase in the coating thickness.

Investigation of cut-edge corrosion behaviour

The SVET and TLM were utilized to study the localised cut-edge and surface corrosion performance of ZMA coatings as a function of coating weight. The SVET results include surface normal current density maps, average hourly measured metal loss and accumulative calculated metal loss over 24 h. SVET data was used to plot normal current density maps representing time-resolved intensity and location of anodic and cathodic activities. Blue and red colours in SVET maps are indicative of cathodic and anodic activities respectively. The SVET-derived metal loss was used to compare the samples however it does not correspond to the exact metal loss for the experiments. As Zn is the predominant element of the ZMA coating, it was chosen during the metal loss calculations.

Table 2 | Average zinc dendrites volume fraction for different ZMA coatings weights samples through the coating thickness

Sample	Zn phase volume %	Eutectic phase volume %
ZMA80	84.03 ± 2.73	15.97 ± 2.73
ZMA200	65.19 ± 6.12	34.81 ± 6.12
ZMA310	70.87 ± 7.61	29.13 ± 7.61

Table 3 | Average zinc dendrites size and surface area fraction for different ZMA coating weights

Sample	ZMA80	ZMA200	ZMA310
Average primary Zn size (μm²)	115	353	363
Zn surface area %	70.1	55	50
Eutectic surface area %	29.9	45	50

Figure 2 shows the SVET normal current density maps measured above the cut-edge surface of ZMA80, ZMA200 and ZMA310 freely in 0.17 M NaCl pH 7 for 1 h, 6 h, 12 h, 18 h and 24 h. In all three samples, cathodic (blue) and anodic (red) activities were detected from the initial scans (1 h scans). In all three samples, anodic activity was detected on the metallic coating layer (ZMA layer) therefore, acting sacrificially to protect the steel substrate. The anodic current was distributed as numerous active local anodes displaying peak anodic current densities of approximately 8 $A.m^{-2}$. The cathodic activity was detected above the steel substrate. Throughout the 24-h experiment, the steel remained cathodically protected.

To quantify the effects of changes in coating weights, the SVET-derived metal losses from the cut-edges were calculated for all three ZMA after immersion in 0.17 M NaCl for 24 h and shown in Table 4. The errors shown are based on the standard deviation of three measurements. The derived

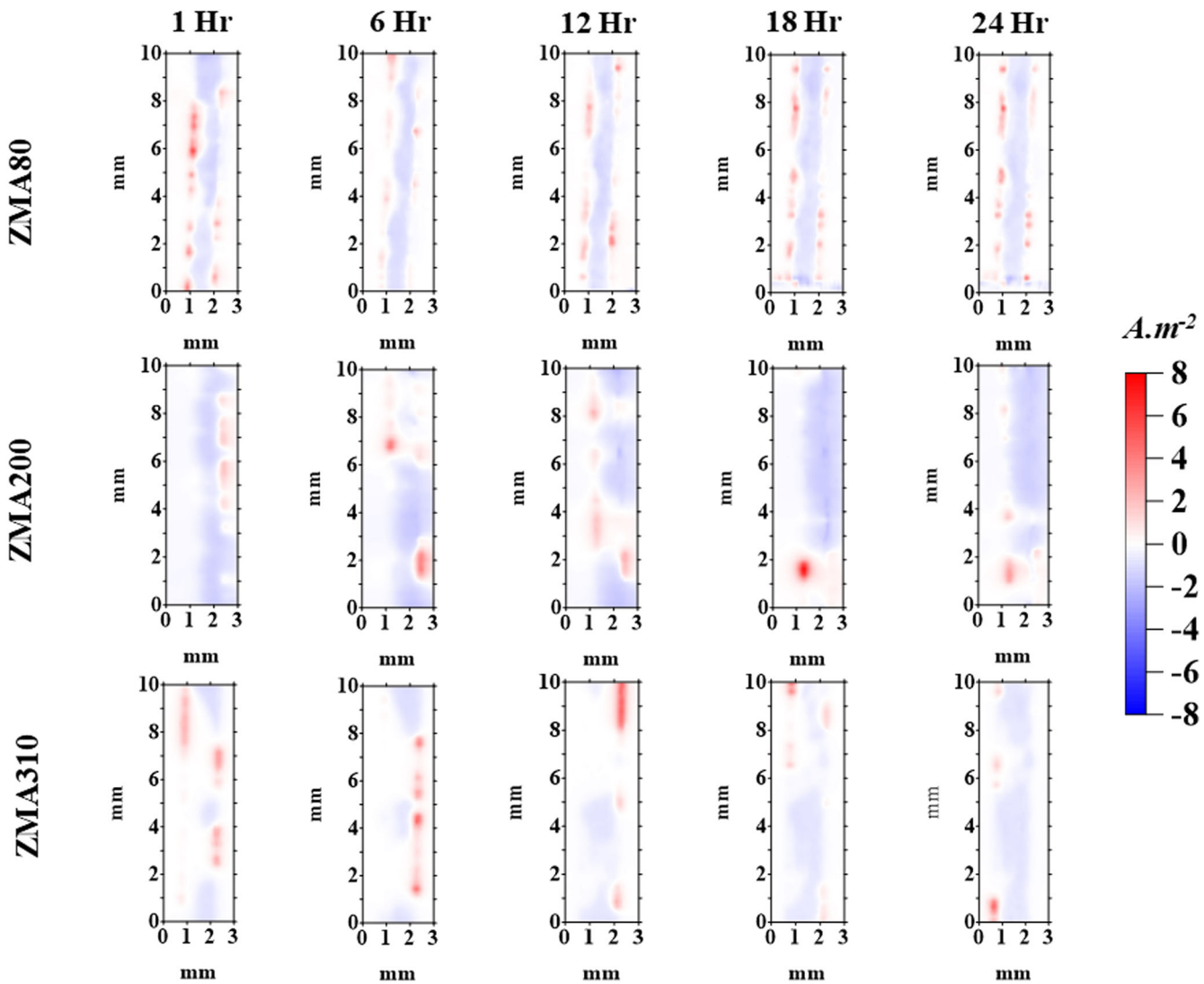

Fig. 2 | SVET false colour maps representing normal current density measured above cut-edges of ZMA80, ZMA200 and ZMA310 immersed in 0.17 M NaCl pH 7 solution for 24 h. Anodic activity is displayed as red and cathodic activity as blue.

metal loss was 0.15 mg, 0.11 mg and 0.13 mg for ZMA80, ZMA200 and ZMA310 respectively.

The SVET-derived hourly metal losses as a function of time for ZMA80, ZMA200 and ZMA310 measured during immersion in 0.17 M NaCl pH 7 solution for 24 h are shown in Fig. 3. The figure represents the maximum and minimum metal loss measured at each hour over three experiments for each ZMA sample. Figure 3 shows that for the first 5 h, the corrosion rate was higher for the thinnest coating (ZMA80) compared to thicker coatings (ZMA200 and ZMA310). However, from the 6th hour onwards the corrosion rate for all three coatings was similar as hourly metal losses seemed to overlap each other. This initial higher corrosion rate on thinner coating may have resulted in a slightly higher SVET-derived metal loss for the thinnest ZMA80 over 24 h. Hence, considering cumulative metal loss for 24 h (Table 4) and corrosion rate (Fig. 3) suggests the variation in coating thickness (weights) does not appreciably affect the total mass loss observed at the cut-edge for these ZMA coatings.

Table 4 | SVET-derived metal loss from the cut-edge of ZMA samples after immersion in 0.17 M NaCl pH 7 for 24 h

Sample	Metal loss (mg)
ZMA80	0.15 ± 0.05
ZMA200	0.11 ± 0.03
ZMA310	0.13 ± 0.06

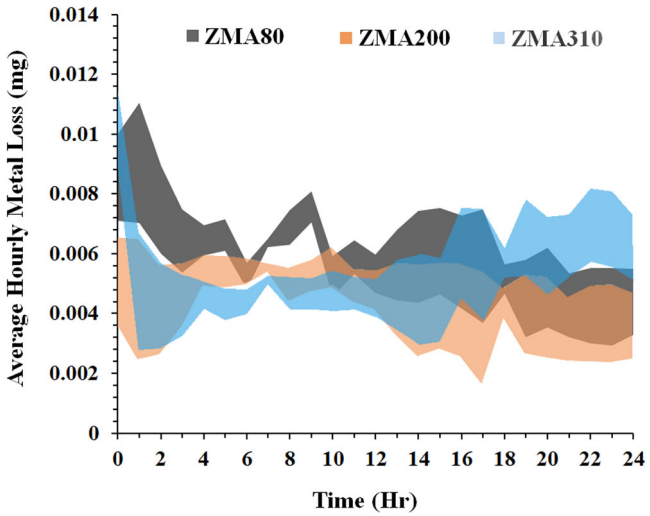

Fig. 3 | SVET measured time-dependent hourly metal loss for cut-edges ZMA samples after immersion in pH 7 0.17 M NaCl solution for 24 h. The ranges represent the maximum and minimum metal loss measured at each hour over three experiments for each ZMA sample.

The corrosion behaviour of ZMA coatings was further investigated using TLM as it enables the acquisition of mechanistic information on a microstructural level with respect to time. As the SVET investigation suggested no significant differences between the coatings in terms of mass loss measured at the cut-edges, the two extremes, the thinnest coating (ZMA80) and the thickest coating (ZMA310) were selected for TLM investigation. The cut-edge TLM experiments were conducted for 12 h in 0.17 M NaCl pH 7 solution. To simulate cut-edge corrosion a consistent semi-circular area of steel surface attached to a layer of ZMA coating was exposed to the electrolyte.

Figure 4 shows optical microscope images of cut-edge surfaces of ZMA80 and ZMA310 at various times of immersion. The figure presents the images captured at 10 min, 30 min, 50 min and 70 min. For both ZMA80 and ZMA310, the anodic attack on the ZMA layer was observed from the onset (Fig. 4, Video 1 and Video 2). Figure 4, Video V1 and Video V2 show that the rate of lateral spreading of the anode through the exposed length of the ZMA layer was relatively slower for thicker ZMA310 compared to thinner ZMA80. In both cases, the anodes grew with respect to time and corrosion products were precipitated in the form of a semi-circle on the steel substrate. Furthermore, the corrosion product ring thickened with time and the exposed steel surface was cathodically protected within the time frame of the experimental time of 12 h with no anodic activity observed.

Figure 5 shows a TLM image of ZMA310 after 30 min of immersion in pH 7 0.17 M NaCl solution. This permits us to examine the behaviour at the cut edge in further detail. An anode had initiated and propagated along the ZMA coating. Additionally, the corrosion product had precipitated as a ring at a certain distance away from the anode where the ionic concentration is such that the solubility product of the salt such as $Zn(OH)_2$ is exceeded. It has previously been suggested the ring indicates the intersection point between the hydroxide ions produced at cathodic sites and the metal ions released from the anodic site[17]. An interesting observation is that within the corrosion product ring, little to no anodic behaviour or corrosion product precipitation was observed with the steel surface remaining precipitation-free.

Investigation of surface corrosion behaviour

The SVET was utilised to investigate the surface corrosion behaviour of ZMA80, ZMA200 and ZMA310. Figure 6 shows the normal current densities detected above the surface of (A) ZMA80 (B) ZMA200 (C) ZMA310 freely corroding in 0.17 M NaCl pH 7 solution for 1 h, 6 h, 12 h, 18 h and 24 h. Peak normal current densities of 5 $A.m^{-2}$ were recorded. For all three samples, anodic activity (Red) and cathodic activity (Blue) were detected

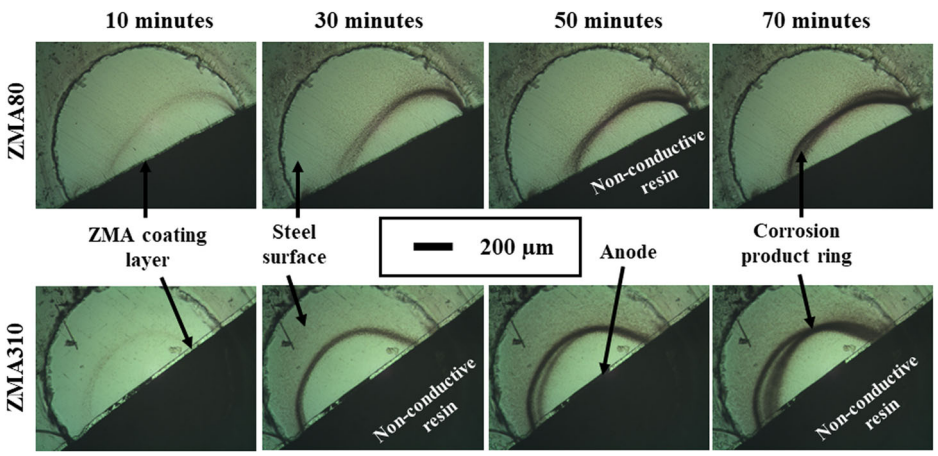

Fig. 4 | Time-lapse Microscope cut-edges images of ZMA80 and ZMA310 under immersion conditions in pH 7 0.17 M NaCl. The images shown were taken at 10 min, 30 min, 50 min and 70 min respectively.

from the onset (1 h scans) and grew radially in size with respect to time. However, a difference in the anode growth mechanism was observed between ZMA80 and ZMA210 / ZMA310.

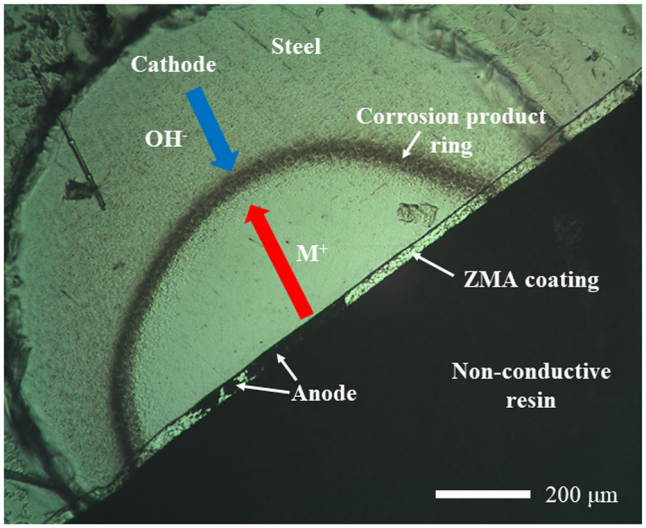

Fig. 5 | Time-lapse Microscope image of cut-edge corrosion of ZMA310 coated steel after 30 min immersion in 0.17 M NaCl pH 7 solution.

For ZMA80, the anodes were mobile as the size and location varied with time with migration over the surface. The anode established at the beginning of the experiment (I, marked on the 6 h SVET colour map, Fig. 6) had passivated by 18 h. For the ZMA200 and ZMA310 coatings anodes did not show the same mobile behaviour and once initiated generally remained fixed in place but grew around this fixed point. For example, the anodes (II and III), marked on 6 h SVET colour maps, in Fig. 6 grew radially in size with increased intensity with time but did not track across the sample surface in the same way as for ZMA80.

The SVET-derived metal losses for ZMA80, ZMA200 and ZMA310 after immersion in pH 7 0.17 M NaCl solution for 24 h are shown in Table 5. The errors shown are based on the standard deviation of three measurements. For ZMA200 the derived metal loss was 29% lower than ZMA80 and for ZMA310 the derived metal loss was 64% lower than ZMA80. Therefore, it suggested a significant performance enhancement for ZMA310 compared to ZMA80.

Table 5 | SVET-derived metal loss from ZMA surfaces after immersion in 0.17 M NaCl pH 7 solution for 24 h

Sample	Metal loss ($g.m^{-2}$)
ZMA80	6.69 ± 1.75
ZMA200	4.74 ± 1.87
ZMA310	2.40 ± 1.15

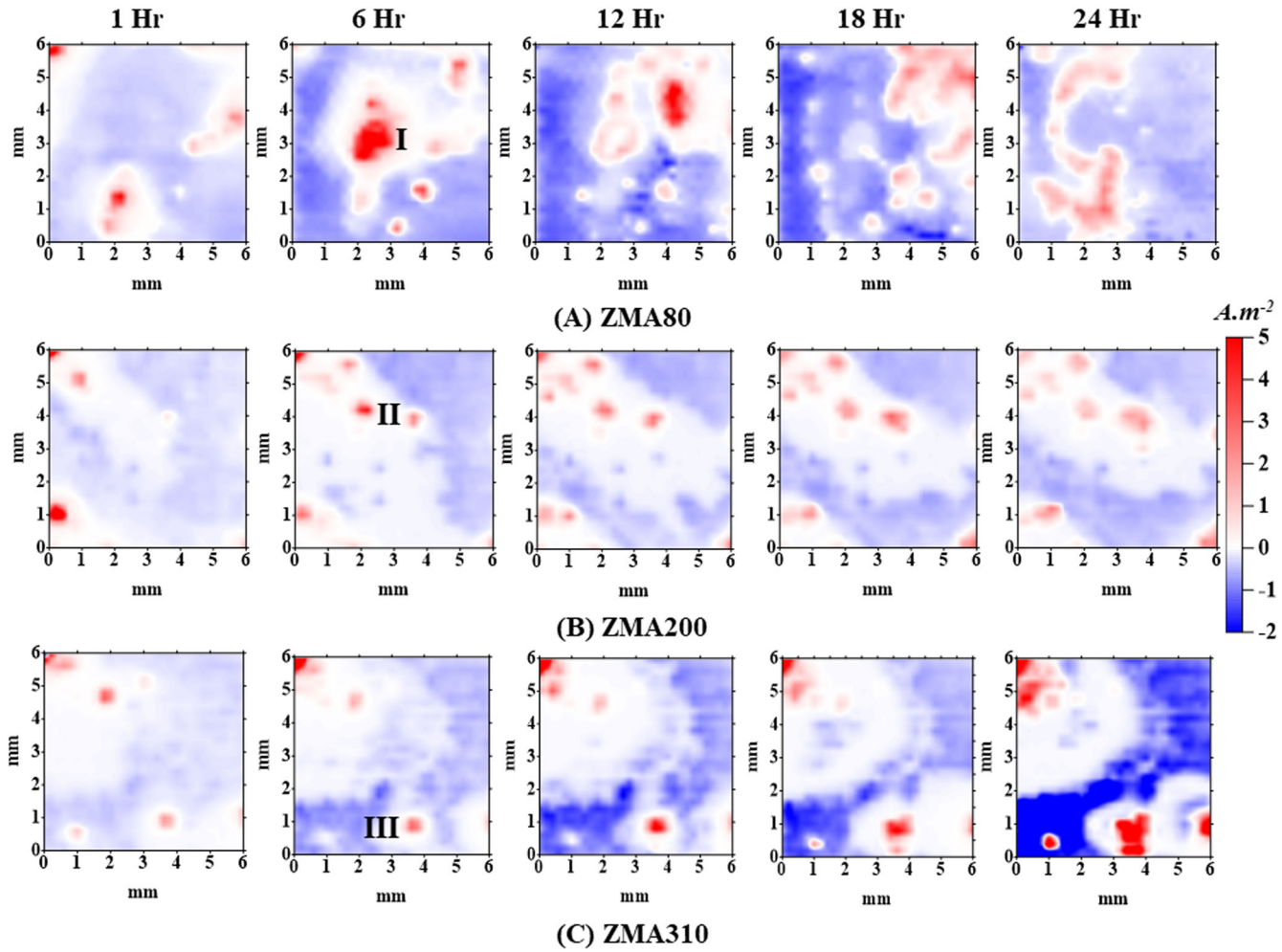

Fig. 6 | SVET false colour maps representing normal current density measured above ZMA surfaces immersed in 0.17 M NaCl pH 7 solution for 24 h. The maps presented are of 1, 6, 12, 18 and 24 h of immersion time for **A** ZMA80, **B** ZMA200 and **C** ZMA310. Anodic activities are shown in red with a maximum of 5 A m^{-2} and cathodic activities in blue with a maximum of −2 A m^{-2}.

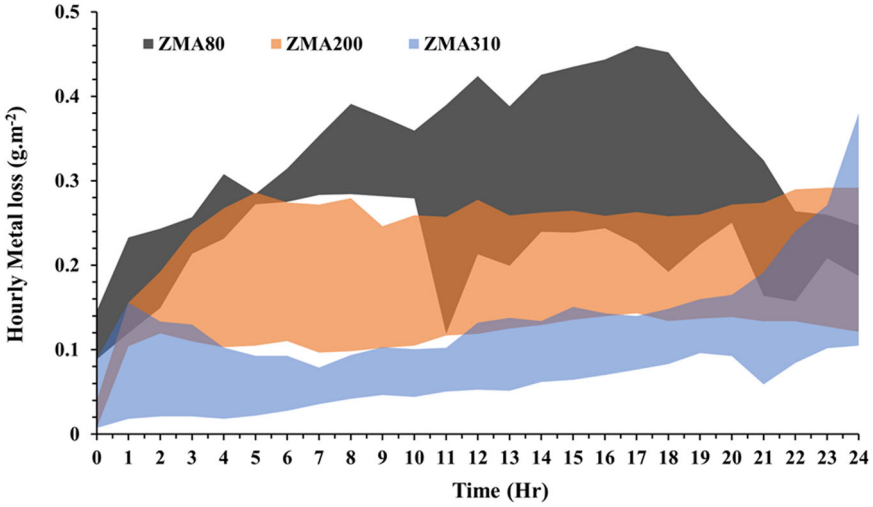

Fig. 7 | SVET derived hourly metal loss as a function of time for ZMA surfaces after immersion in pH 7 0.17 M NaCl solution for 24 h. The ranges represent the maximum and minimum metal loss measured at each hour over three experiments for each ZMA sample.

The SVET-derived hourly metal losses as a function of time for ZMA80, ZMA200 and ZMA310 during immersion in 0.17 M NaCl pH 7 for 24 h are shown in Fig. 7. The figure represents the maximum and minimum metal loss measured at each hour over three experiments for each ZMA sample. For ZMA80, a gradual linear increase in metal loss was observed for the first 6 h followed by a plateau. For ZMA200 and ZMA310, the rate the metal loss was unchanged for the majority of the experimental time however ZMA310 displayed an increased corrosion rate towards the end. The figure shows ZMA80 consistently displayed the highest metal loss at each hour followed by ZMA200 and then ZMA310, hence, suggesting improved corrosion resistance as coating weight is increased.

Open Circuit Potential (OCP) and Linear Polarization Resistance (LPR) were performed to further investigate the influence of the coating thickness of ZMA coatings on the surface corrosion behaviour. The measurements were initiated immediately after the introduction of the electrolyte. OCP is the potential of the working electrode (material under investigation) measured over time with respect to the reference electrode in a given electrolyte. As no external voltage is applied, the net current flow is equal to zero. LPR measurements have come to be a well-established method of establishing the corrosion rate of a corroding material. It is the ratio of applied potential to the resulting current response. During measurement, a small potential perturbation was applied in a step-wise manner, commencing at − 15 mV vs SCE below the OCP and ending at + 15 mV vs SCE above the OCP.

Figure 8A shows the OCP measurements of ZMA coatings immersed in pH 7 0.17 M NaCl over 24 h. The initial potential was ~ −1.004 ± 0.002 V vs SCE for the ZMA coatings after which a shift to more negative potential was observed. This negative shift in the potential was similar for ZMA200 and ZMA310. However, for ZMA80, the negative shift was greater compared to both ZMA200 and ZMA310. All three ZMA coatings obtained a relatively stable potential after ~ 14 h of immersion. A relationship between the coating thickness and this relatively stable potential can be observed in Fig. 8A. The relative stable potential value increases with the increase in coating thickness. For ZMA310, the relative stable potential is ~1.016 V vs SCE compared to ~1.02 V vs SCE for ZMA200 and ~1.04 V vs SCE for ZMA80 after 14 h of immersion. This indicates that ZMA310 has the highest thermodynamic stability of the three coating weights investigated.

LPR data has been presented as polarisation resistance (R_p) values and illustrates the rate of corrosion[25]. Figure 8B shows the R_p values of ZMA coatings immersed in pH 7 0.17 M NaCl over 24 h. The R_p values of ZMA200 were higher than ZMA80 therefore, indicating ZMA200 provided better protective ability compared to ZMA80 as $i_{corr} \alpha 1/R_p$. However, the R_p values of ZMA310 were significantly higher compared to both ZMA80 and ZMA200. For the first 10 h, R_p values of ZMA310 were ~ 3 times higher compared to both ZMA80 and ZMA200.

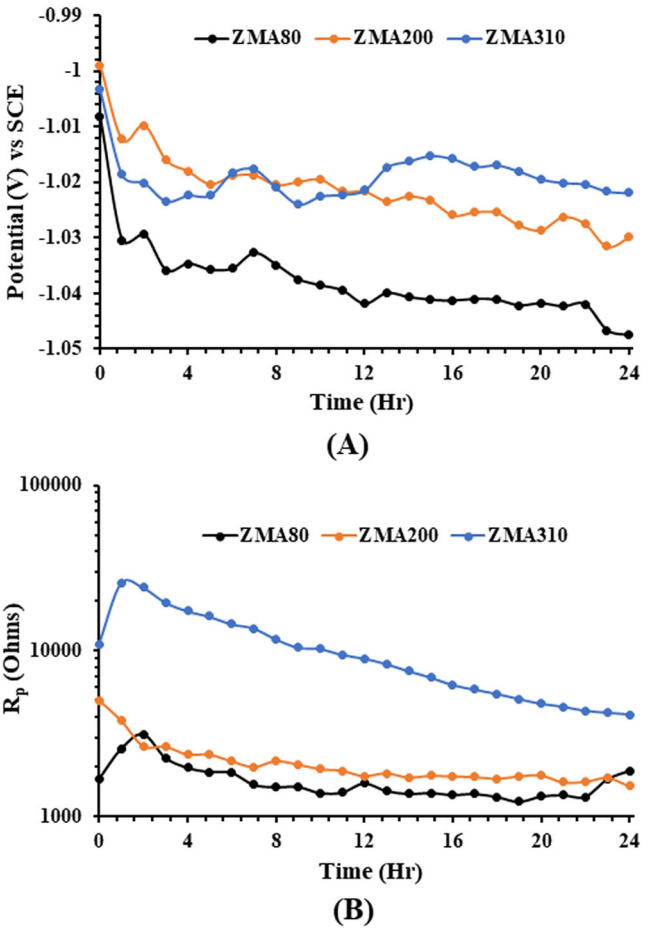

Fig. 8 | The time-dependent OCP and polarisation resistance for ZMA samples immersed in pH 7 0.17 M NaCl for 24 h. The **A** OCP and **B** polarisation resistance values increased with the increase in coating thickness.

The surface corrosion of ZMA coatings was further investigated using TLM. TLM enables the in-situ investigation of corrosion mechanisms under immersion conditions at the microstructural level. Here, only the TLM images and TLM videos of ZMA80 and ZMA310 are

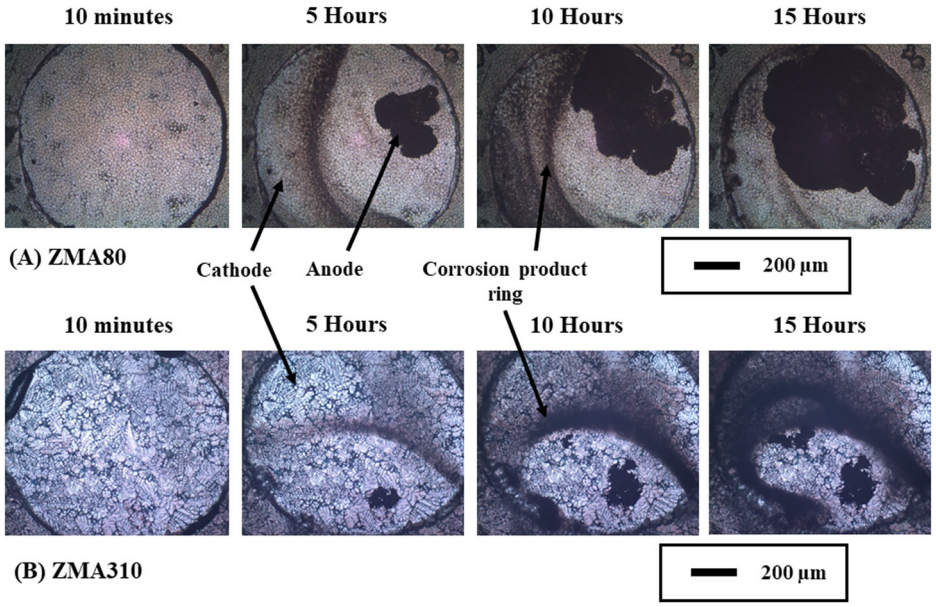

Fig. 9 | Time-lapse microscope images of ZMA surfaces taken in situ under immersion conditions in pH 7 0.17 M NaCl solution. The images shown were taken at 10 min, 5, 10 and 15 h for both **A** ZMA80 and **B** ZMA310. The images show the development and progression of the anodic areas and the corrosion product rings with respect to time.

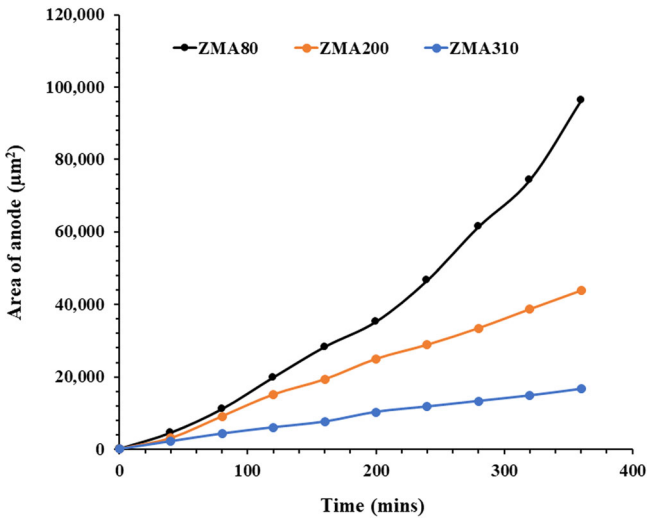

Fig. 10 | Plot of the corroded area as a function of time for ZMA samples with various coating weights.

Table 6 | Anode area after 6 h immersion in 0.17 M NaCl pH 7 solution for ZMA samples

Sample	ZMA80	ZMA200	ZMA310
Corroded area (µm²)	96,496	43,843	16,680

presented because ZMA200 and ZMA310 demonstrated similar microstructure (Fig. 1, Tables 2, 3) and similar corrosion mechanisms on SVET investigation (Fig. 6).

Figure 9 shows optical microscopy images of the surfaces of ZMA80 and ZMA310 after various times of immersion in pH 7 0.17 M NaCl. The figure presents the images captured at 10 min, 5 h, 10 h and 15 h. For ZMA80, an anode (presenting as a black region) is initiated in the upper right quadrant of the exposed area and then spread across the surface of the exposed surface with respect to time (Fig. 9A and Video V3). For ZMA310, an anode was initiated in the lower right quadrant of the exposed area and then grew radially with respect to time, however, the spread of the anode was much more constrained (Fig. 9B and Video V4). At 10 h a second anodic feature also initiated to the left of the initial anode and again grew in size with respect to time. These observations align well with the spatial and time-resolved data captured by the SVET (Fig. 6) where a similar mechanism was observed for anodic growth.

To demonstrate the difference in corrosion behaviour between the ZMA samples, the corroded (anode) area with respect to time for 6 h is presented in Fig. 10 and Table 6. It should be stated that measurements taken are 2D as they come from image analysis of 2D images hence, the penetration into the coating thickness cannot be measured. Nevertheless, the trend in performance aligns with the two electrochemical tests (SVET & LPR) discussed in sections 2.2.2.1 and 2.2.2.2. A plot of the corroded area as a function of time and total corroded area after 6 h of immersion in 0.17 M NaCl pH 7 for ZMA80, ZMA200 and ZMA310 are presented in Fig. 10 and Table 6, respectively.

Figure 10 demonstrated a linear increase in the corroded area for all three samples however the rate of corrosion increased with a decrease in coating thickness. ZMA80 displayed the highest corroded area of 96,496 µm² after 6 h of immersion in 0.17 M NaCl pH 7 solution. The total corroded area for ZMA200 and ZMA310 after 6 h immersion in pH 7 0.17 M NaCl are 43,843 µm² and 16,680 µm² respectively. Hence, a decrease in the total corroded area was observed with the increase in coating thickness.

Relationship between SVET metal loss and TLM corroded area

To further develop a mechanistic understanding of the relationship between the surface corrosion behaviour and the coating surface microstructure, the quantified corrosion data (SVET and TLM) was plotted against the microstructural data (average primary Zn size and area fraction of primary Zn). The SVET-derived metal loss (24 h) and TLM corroded area (6 h) were plotted against the average primary Zn size and area fraction of the primary Zn phase and are presented in Fig. 11.

Figure 11A shows both SVET-derived metal loss (orange square dots) and TLM corroded area (blue circular dots) decrease with an increase in primary Zn dendrite size. Figure 11B shows both SVET-derived metal loss (orange square dots) and TLM corroded area (blue circular dots) increase with an increase in the area fraction of the primary Zn phase. It can also be observed an approximately linear relationship occurs between the area fraction of the primary Zn phase and the corroded area of TLM and SVET-derived metal loss. This indicates that both the size and area fraction of the primary Zn phase influence the rate of corrosion on the ZMA coatings.

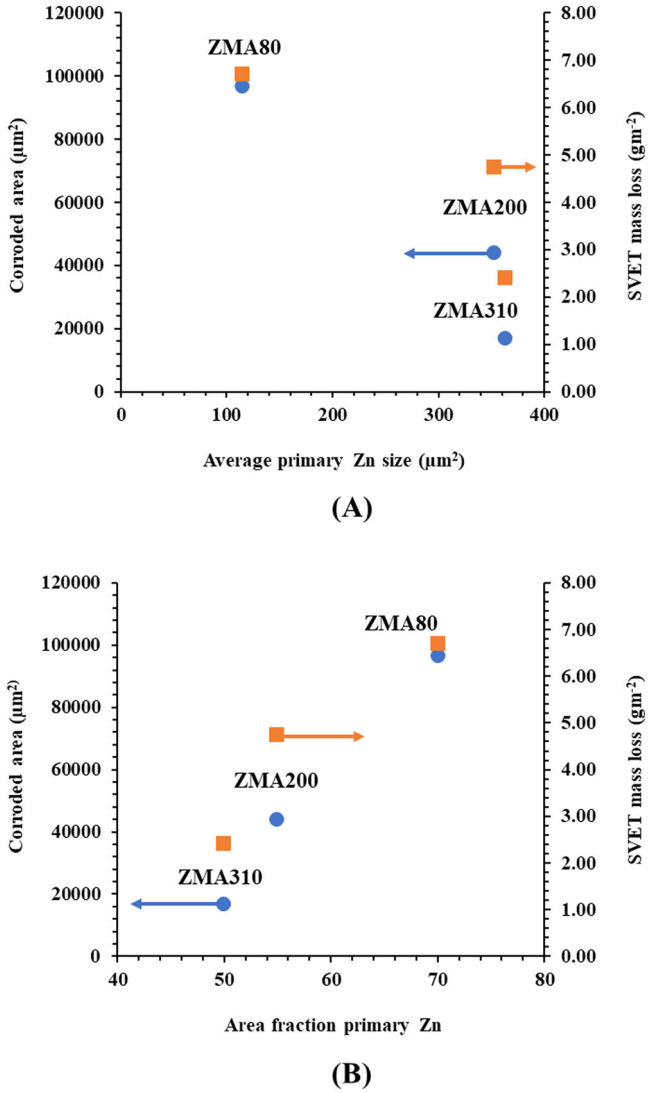

Fig. 11 | Relationship between SVET-derived metal loss and TLM corroded area against ZMA microstructure. The corrosion resistance improved with the increase in **A** average primary Zn size, whereas the corrosion resistance declined with an increase in **B** the area fraction of primary Zn.

Table 7 | Elemental quantification of ZMA80 and ZMA310 using inductively coupled plasma mass spectrometry (ICP-MS)

Sample	Zn (wt.%)	Mg (wt.%)	Al(wt.%)
Bath Chemistry	Bal.	1.48	1.72
ZMA80	Bal.	0.90	1.33
ZMA310	Bal.	1.47	1.64

Discussion

Microstructural analysis revealed that changes in coating weight led to significant modifications in the coating microstructure with the surface area fraction and through coating volume fraction of the primary Zn phase decreasing as coating weight increased. Furthermore, the average size of individual primary Zn phases increased as the coating weight increased. These changes occurred due to the different cooling rates experienced by the coatings as a function of weight/thickness. Lower coating weights require higher pressures in the gas knives in order to remove more liquid metal. This imparts higher cooling rates and hence less time for the growth of solidifying phases leading to a refined microstructure. For higher coating weights, the cooling rate is reduced with more time for the growth of phases resulting in coarser microstructures. The change in volume fraction of the phases is an interesting phenomenon given that the coatings all had the same composition since they were made during the same process campaign with the same galvanising bath and conditions, other than gas knife changes to effect the coating weight differences. For the lowest weight coating, ZMA80, the increase in primary Zn and converse reduction in eutectic phases could theoretically be achieved, from a compositional point of view, by increasing the freezing range. In practice, this could be achieved through increased undercooling from high cooling rates or a reduction in the wt.% of Mg and Al. Figure 12 shows EDX line scans for ZMA80 and ZMA310 coatings to evaluate the elemental distribution within the primary Zn phase that is first to solidify. If the observed volume fraction change for ZMA80 was due to high cooling rates inducing solute retention in the primary phase, there would likely be a compositional change across the dendrites due to coring. This was not observed in the EDX scans presented in Fig. 12 and therefore retention of solute is unlikely to be responsible for the observed volume fraction differences.

ZMA80 was produced using a significantly higher wiping knife pressure than the ZMA310 therefore it is postulated that the act of wiping at high pressure can cause temporary cooling in the wiping zone potentially leading to nucleation of the primary phase. This would result in solute-rich liquid being removed back into the bath resulting in a final solidified coating that contains less Mg and Al than the bath chemistry. This phenomenon has been previously observed in low coating weight Zn – 4.8 wt. % Al coatings[22,26]. Elsaadawy et al. published a coating weight model predicting heat transfer in the galvanising process[27]. The model predicted 80% solidification for 130 g.m^2 Zn coating within 15 m of the gas knives. Additionally, the model predicted heat transfer coefficients at the narrow wiping zone approaching 1000 W.m^{-2}.K^{-1}. In this paper, the solidification point was derived through visual observations of the "dry line" where there is a visual change in surface appearance. However, this does not consider solidification in the knives followed by re-melting. It also does not consider solidification at the steel/coating interface as the visual observation considers the coating surface. Therefore, it is postulated here that some nucleation is occurring in the wiping zone which is sufficient to modify the final coating composition. Previous observations in Zn - 4.8 wt. % Al showed that thinner coatings displayed reduced Al levels as measured by coating digestion and ICP-MS[22]. Table 7 presents compositional information for ZMA80 and ZMA310 coatings measured using coating digestion and ICP-OES from an independent laboratory (Element Materials Technology, Sheffield). These data show a drop in both Mg and Al concentrations in the ZMA80 coating in comparison to ZMA310 and the bath composition. This supports the theory of some solidification of primary Zn in the wiping zone and removal of solute-rich liquid back into the bath resulting in a final, leaner alloy chemistry for thin coatings. This explains the drop in eutectic volume fraction for ZMA80 as shown in Tables 2, 3.

At the cut-edge, a galvanic couple occurs between the exposed steel substrate and the applied ZMA coating, hence providing cathodic protection. Due to the potential difference between the steel substrate and ZMA coating, the anodic reactions occurred on the ZMA coating that has the more negative potential and the cathodic reactions take place on the nobler steel substrate. The anodic attack on the coating appeared indiscriminate of the microstructural phases due to cathodic activity becoming focussed on the steel and thus, the anodic reactions led to the dissolution of metal/intermetallics to metal ions (Zn^{2+}, Al^{3+} and Mg^{2+}) with the cathodic oxygen reduction reaction (ORR) on the steel substrate producing OH^- ions (Eqs. (1)–(4)).

$$Zn \rightarrow Zn^{2+} + 2e^- \quad (1)$$

$$Al \rightarrow Al^{3+} + 3e^- \quad (2)$$

$$Mg \rightarrow Mg^{2+} + 2e^- \quad (3)$$

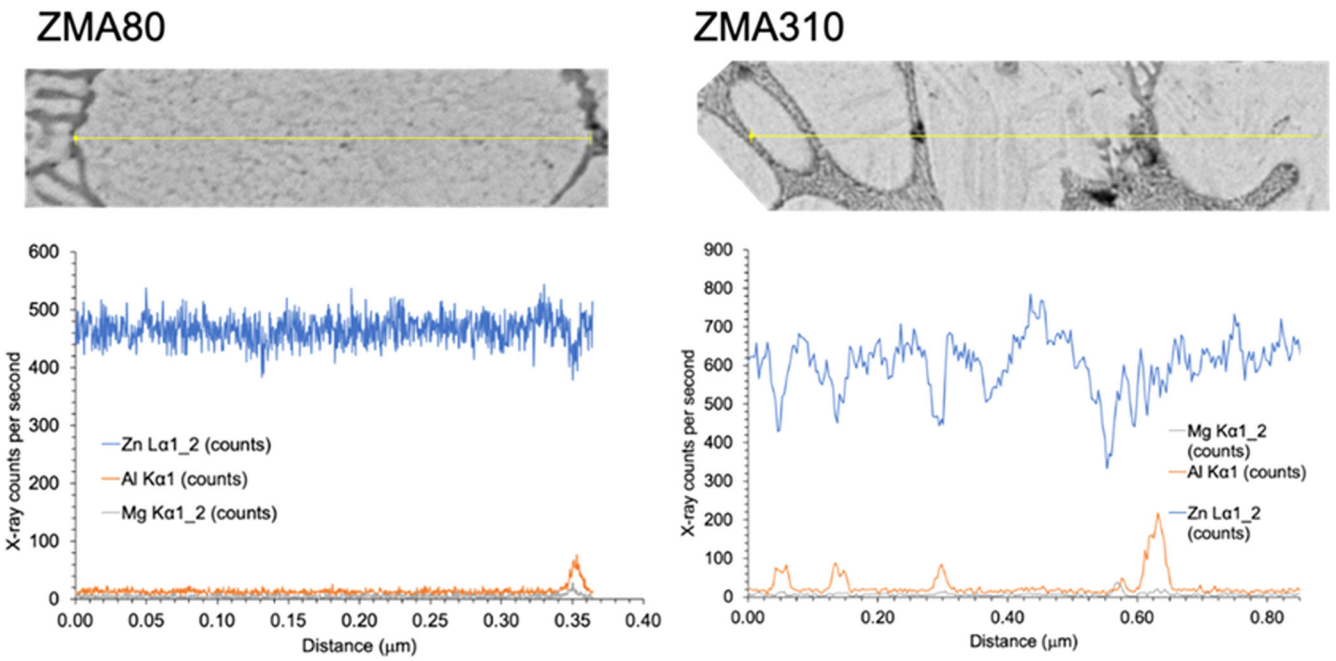

Fig. 12 | EDX line scans for ZMA80 and ZMA310 coatings to evaluate the elemental distribution within the primary Zn phase.

Fig. 13 | Methods of anode growth controlled by dendrite size. The anode **A** trans-propagation mechanism was observed for ZMA80, whereas the anode **B** contiguous propagation mechanism was observed for the ZMA200 and ZMA310.

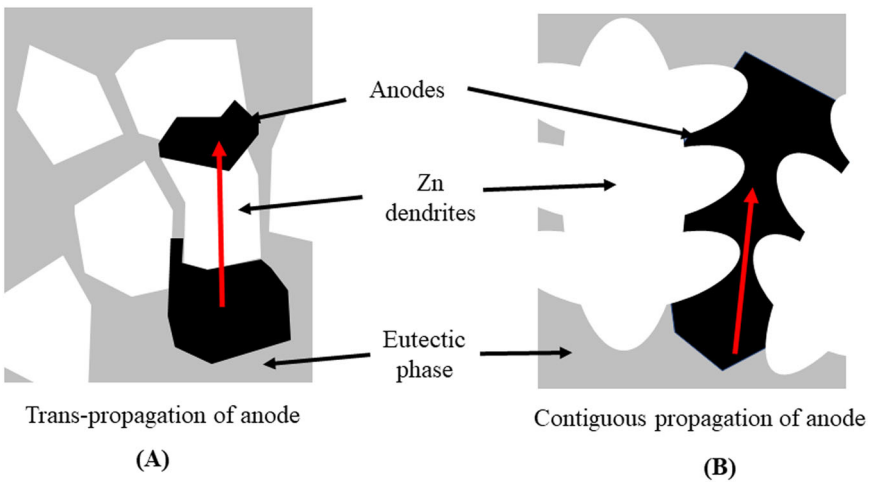

$$O_2 + 2H_2O + 4e^- \rightarrow 4OH^- \quad (4)$$

Due to the galvanic coupling and the large surface area ratio of the steel substrate with respect to the ZMA coating, the anodic growth rate in ZMA coatings was increased compared to surface corrosion. ZMA80 demonstrated the highest corrosion rates over the initial hours of the experiment due to the thinner coating displaying the highest current density. However, with time the corrosion rate for all three coatings was similar within experimental error and this was thought to be controlled principally by the ORR becoming diffusion-limited due to the consumption of oxygen at the cathodic areas of the samples[28,29]. Hence, a similar corrosion rate for all three ZMA coatings was observed after the initial 6 h.

TLM demonstrated a "semi-circular" precipitation of corrosion products on the steel surface at a radius away from anodes in the ZMA layer. The precipitation of corrosion products is governed by their solubility product constant (K_{sp}). Precipitation will occur when the solution pH and metal ion concentration levels are such that K_{sp} is exceeded. The semi-circular corrosion product ring is thus an indication of where such conditions have been met on the ZMA-coated steels tested. The highest concentration of metal ions would be expected close to the anode with subsequent radial migration and diffusion towards the steel cathode leading to a reduction in metal ion concentration with radial distance from the anode. The lack of corrosion products close to the anode may be due to changes in the local pH. As stated previously, the anodic attack of the coating at the cut edge was relatively indiscriminate of microstructural phases and as such there was potential for the production of Zn^{2+}, Mg^{2+} and Al^{3+} ions into solution at an anode. Considering these ions in solution, both Zn^{2+} and Al^{3+} will undergo hydrolysis locally reducing the pH in solution whereas the Mg^{2+} ions do not readily hydrolyse[30]. As such this local reduction in pH will increase the solubility of the corrosion products and no precipitation will occur close to the anode as observed in the TLM images (Figs. 4 and 5). Conversely, over the steel surface where cathodic oxygen reduction is occurring, an alkaline pH will be found due to OH^- production (Eq. 4). OH^- will migrate and diffuse towards the anode. The counter-current of OH^- ions from the cathode and metal ions from the anode will eventually create

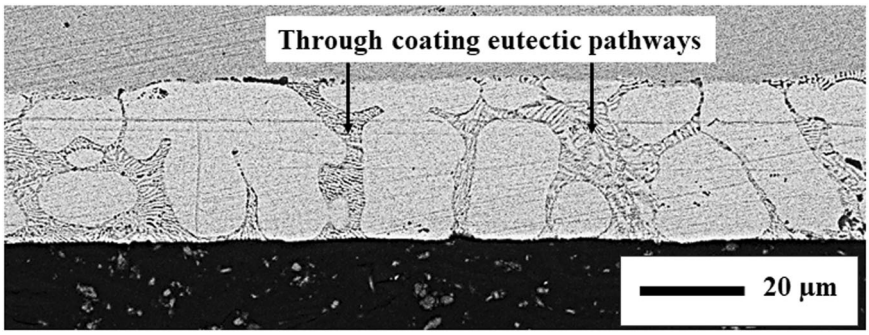

Fig. 14 | Cross-section of ZMA coating showing evidence of through-coating eutectic pathways.

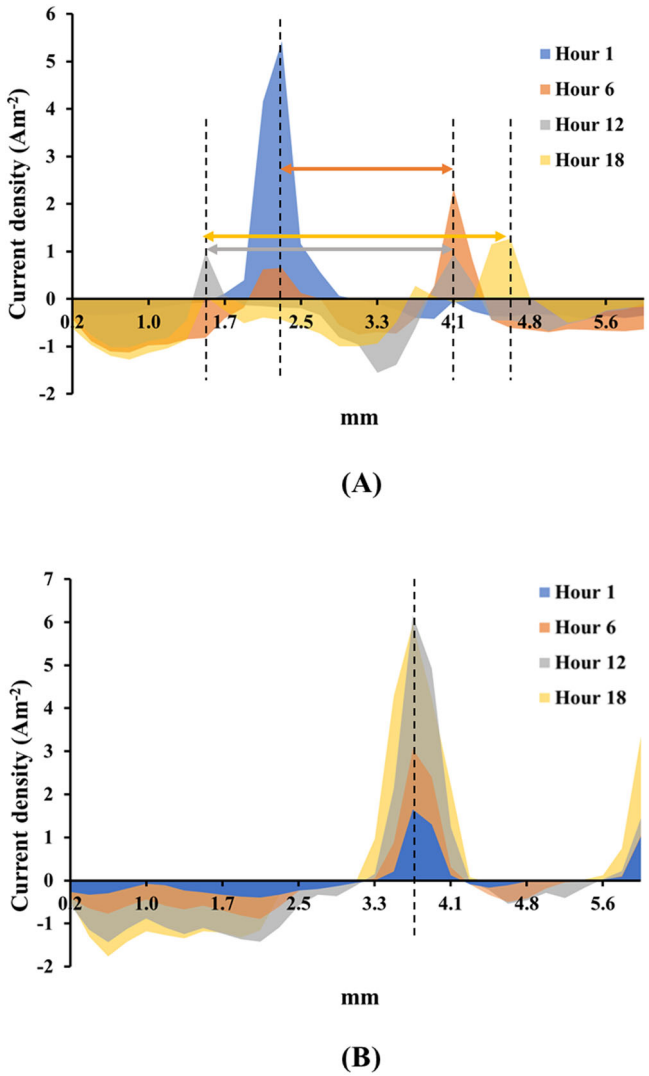

Fig. 15 | SVET recorded current density measured across a typical anodic site over 18 h of immersion in 0.17 M NaCl pH 7 showing anodes lateral spreading and deactivate mechanism. The anodes spread laterally with respect to time for (**A**) ZMA80 but stay fixed and become more intense for (**B**) ZMA310.

conditions in the solution with regards to ion concentration and pH favourable for the precipitation of corrosion products and this appears as a ring some distance from the anodic site.

This investigation showed that the surface corrosion performance improved with an increase in coating weight/thickness (ZMA80 to ZMA310). There are several possible reasons why thicker coatings (ZMA310) displayed better corrosion resistance than thinner coatings (ZMA80).

- The higher surface volume fraction of primary Zn in ZMA80 meant that there were lower levels of Mg and Al phases at the surface compared to thicker coatings. Previous work has demonstrated that in ZMA, anodes initiate at the active $MgZn_2$[17] within the eutectic phases that have a potential of -1.41 V vs SCE[31,32]. Anodes then grow preferentially via the eutectic phase through galvanic dissolution of the $MgZn_2$ component with cathodic activity occurring on the primary Zn phases. The Mg^{2+} ions released from this anodic attack tend not to hydrolyse in solution and consequently, the pH of the electrolyte adjacent to the sample surface tends to rise enabling the precipitation of Zn and Mg corrosion products thus reducing the corrosion rate. Therefore, less Mg in the surface means less Mg^{2+} in the solution and thus this protective effect of higher pH will be reduced.
- A further consequence of less Mg and Al at the surface will mean that Zn will increasingly undergo anodic attack as more of the surface is Zn-rich. More Zn^{2+} will be released that will hydrolyse reducing the pH promoting further anodic attack and reduced passivation from corrosion product formation. This can be seen in Fig. 9A where the corrosion products that have formed on the surface of ZMA80 in the left-hand side of the exposed circle of material after 10 h become solubilised by hour 15 as the anode progresses across the surface towards this area. In ZMA310 in Fig. 9B the corrosion products do not experience a similar solubilisation perhaps indicative of reduced hydrolysis in solution due to the higher Mg levels present at the sample surface.
- Reduced Al levels at the surface will result in less enrichment of Al_2O_3 at the alloy surface. Al_2O_3 is a dense, protective wide band gap oxide that increases corrosion resistance and hence lower levels of Al_2O_3 at the surface of ZMA80 may permit a higher corrosion rate.
- Zn is a more kinetically efficient surface for supporting the cathodic oxygen reduction reaction than the eutectic phases[33]. Therefore, the ZMA80 surface that is richer in Zn, especially in condensed sites, such as primary Zn dendrites, can support increased cathodic activity, which is often the rate-determining reaction in a corrosion system where oxygen reduction is occurring.

The overall corrosion rate is obviously a critical consideration for these coatings but the spatial and temporal distribution of corrosion features should also be considered. The TLM and SVET data revealed a change in corrosion mechanism between the lowest and highest weight coatings. TLM revealed that anodes spread over the surface for ZMA80 but in contrast, were more localised and constrained for ZMA310. Initially, when $MgZn_2$ undergoes preferential anodic dissolution, the Zn dendritic phases become cathodically protected via galvanic coupling leading to anodes preferentially progressing through the eutectic phases. However, once the local eutectic is consumed the Zn dendrites are attacked. Therefore, it is postulated here that the size of the Zn dendrites influences the growth mechanism of anodes with the spreading of anodes potentially occurring via two different methods:

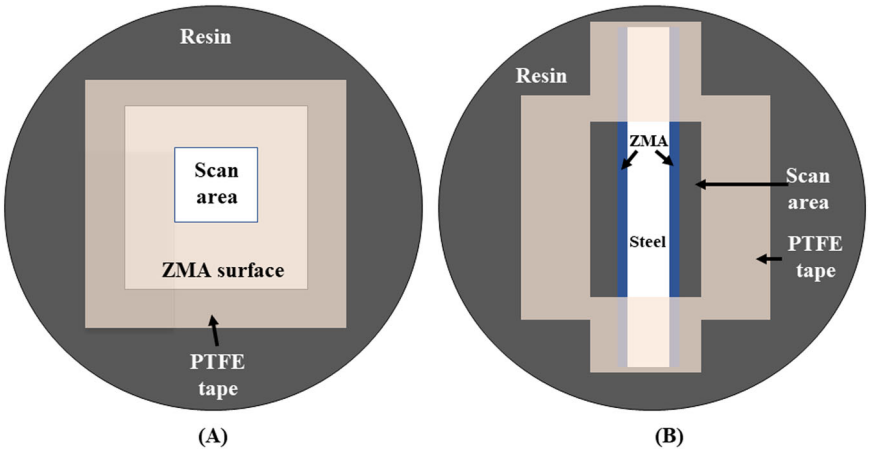

Fig. 16 | Schematic of sample exposure for SVET experiments. (**A**) For surface corrosion experiments a square area of 6 mm x 6 mm and (**B**) for cut-edge corrosion experiments a rectangular cross-sectional area of 3 mm x 10 mm was exposed to 0.17 M NaCl pH 7 solution.

i. Trans lateral propagation across the dendrites—an anode can spread over a dendrite to an adjacent region of eutectic.
ii. Contiguous propagation around the dendrites—anodes pass through the eutectic between and around the dendrites, but do not cross over them.

The schematic of these two different methods is presented in Fig. 13.

The effect of the size of microstructural phases on the ability of anodes to undergo trans-lateral propagation or contiguous propagation has previously been observed in our group where ZMA alloy coatings produced in a hot dip process simulator experienced various cooling rates during solidification[21]. In that work, it was postulated anode growth was controlled by the local anolyte concentration that varies as a function of distance due to hemispherical diffusion of ions away from the anode. The anolyte immediately above an anode will contain Mg^{2+}, Zn^{2+} and Cl^- ions with the presence of Zn^{2+} from eutectic dissolution creating a weakly acidic pH preventing passivation of the alloy. Conversely, the Zn dendrites will support the ORR due to galvanic coupling with the $MgZn_2$ containing eutectic phases and hence will be cathodically protected. The production of OH^- ions from the ORR will enable the pH to rise over this phase encouraging passivation through zinc hydroxide formation. As such, larger dendrites will provide a chemical environment that does not support the trans-lateral propagation of anodes as the concentration of the anolyte will drop below a critical concentration necessary for the continued progression of an anode across a dendrite. Conversely, the anolyte concentration can be maintained above a critical concentration when passing over a smaller dendrite. This mechanism is discussed in further detail in our previous work[21]. Trans lateral propagation was observed in ZMA80 as its microstructure consists of fine and small Zn dendrites (Fig. 1A) and permits the anodes to spread more extensively across the surface as its progression is not restricted by having to track around and between dendrites whereas contiguous propagation of anode was observed in ZMA310 as anodes must progress around the dendrites due to large Zn phases (Zn phases support cathodic activities due to galvanic coupling with eutectic) therefore constraining the rate and extent of lateral spreading.

This difference in anode progression poses a question. Which mechanism is preferable in terms of coating lifetime?

Trans lateral anode spreading in the ZMA80 sample produced the highest anode growth area in TLM, the highest SVET measured mass loss and the highest corrosion rate in LPR all suggesting that this mechanism is less favourable. However, the spreading of anodic activity over the surface may serve to reduce the rate of through-coating penetration to the steel substrate, and therefore accelerated galvanic dissolution, as the anodic attack is not focussed in discrete, localised sites. The more constrained anodes observed for ZMA310 may therefore lead to more rapid through-coating penetration to the steel substrate. Furthermore, considering the image of ZMA310 in Fig. 14 it can be seen that there are multiple through-coating, eutectic pathways to the substrate and thus anodes that initiate at the surface have relatively straightforward progression pathways through to the steel substrate.

As stated, the measured LPR data would suggest that the corrosion performance is worst for ZMA80 with SVET mass loss supporting this. However, the spatial and time-resolved information from SVET provides an opportunity to better interrogate the morphology of the corrosion, not just an overall mass loss/rate. Figure 15 shows the evolution of a typical anodic feature with regard to its intensity and position with respect to time as measured by the SVET. For ZMA80 (Fig. 15A) the anode that initiated at hour 1 with a high current density of approximately 5.5 Am^{-2} consequently laterally spread with respect to time with a subsequent decrease in current density. At hour 6, the anodic front has shifted ~1.5 mm towards the right-hand side from its original position. Conversely, for ZMA310 (Fig. 15B) the anode that initiated at hour 1 remained focused at that location and subsequently became more active with respect to time. This pattern was observed for numerous anodes analysed across multiple samples of both ZMA80 and ZMA310. This, therefore, suggests that for the production of samples with the same coating weight the process should be influenced to produce coatings with smaller dendrites as these encourage the spreading of anodic activity whereas large dendrites encourage focussed anodic activity that could lead to more rapid through coating penetration to the steel substrate. This would effectively shorten the lifetime of the coating as the coating would then corrode at a higher rate due to galvanic coupling with the exposed steel. It is therefore important to use a variety of techniques when assessing the corrosion behaviour of ZMA coatings as the localised morphology of corrosion should be considered in addition to area-averaged electrochemical measurements.

In conclusion, the microstructural and electrochemical investigation has been conducted using a combination of techniques to understand the influence of the coating weight of ZMA coatings and elucidate the corrosion morphology. The investigation showed that;

- Increasing the coating weight led to a modification of the ZMA microstructure from a fine microstructure seen in the 80 $g.m^{-2}$ coating (ZMA80) to a coarse microstructure seen in the 310 $g.m^{-2}$ coating (ZMA310). The average primary Zn dendrite size increased from 115 μm^2 (ZMA80) to 363 μm^2 (ZMA310). The volume fraction of the primary zinc phase reduced from 84.03% (ZMA80) to 70.87% (ZMA310) and conversely the volume fraction of the eutectic phase increased from 15.97% (ZMA80) to 29.13% (ZMA310).
- SVET revealed that coating weight did not appreciably affect the total metal loss observed at the cut-edge over 24 h probably due to Oxygen becoming diffusion-limited at the exposed steel cathode.

- SVET, LPR and TLM revealed an improvement in surface corrosion resistance with an increase in coating weight. A 64% decrease in SVET metal loss was measured for ZMA310 compared to ZMA80.
- SVET and TLM revealed a difference in corrosion morphology between the lowest and highest coating weights. Both techniques showed the anodic growth mechanism on ZMA310 was much more localised and constrained compared to ZMA80. TLM revealed that lateral anodic spreading was constrained and deflected by large Zn dendrites in coarser microstructures (ZMA310). On the contrary, lateral anodic spreading was higher in the presence of small Zn dendrites or fine microstructure (ZMA80).

Methods

Materials

ZMA [(1–2) wt.% Al – (1–2) wt.% Mg – Bal. Zn] coatings were produced on a continuous coil coating line with varying metallic coating weights from 80 $g.m^{-2}$ to 310 $g.m^{-2}$ controlled by altering the gas knife pressure processing parameters. The thinnest coatings require high pressure and closer knife-stripe distance compared to thicker coatings. Line speed and bath temperature were kept constant throughout the production process. DX 51 (0.18 wt.% C, 1.20 wt.% Mn, 0.12 wt.% P, 0.045 wt.% S, 0.30 wt.% Ti, Bal Fe), formable low-carbon steel substrate (TATA Steel) was used for all the coatings.

Chemicals used during the investigation; sodium hydroxide (NaOH), ethanol (C_2H_5OH), nitric acid (HNO_3) and hydrochloric acid (HCl) were purchased from Sigma-Aldrich Chemical Co. and were of analytical grade purity. A 0.17 $mol.dm^{-3}$ NaCl pH 7 (1 wt.% NaCl) solution was used throughout and the pH of the bulk solution was adjusted using aqueous NaOH or HCl.

Microstructural analysis

The samples were hot mounted in non-conductive phenolic resin (Metprep Limited), ground using silicon carbide (SiC) paper to a European P grade P4000 grit finish, polished with aqueous 1 µm diamond suspensions, etched using 3 wt.% Nital and rinsed with distilled water and ethanol. A Meiji Techno MT7100 Metallurgical Optical Microscope and Hitachi TM3000 Scanning Electron Microscope (SEM) with Bruker Energy Dispersive X-ray Spectroscopy (EDS) module were utilized to capture microstructure images and information regarding the quantities and distributions of the constituent elements. The volume fraction of different microstructural phases was determined by image analysis of cut-edge SEM images using Adobe Photoshop software. The size of Zn dendrites and area fraction of both phases (Zn & Eutectic) were determined by image analysis of a circular area of 0.78 mm^2 exposed for TLM experiments using trainable Weka Segmentation, a Fiji plugin. The image analysis software was spatially calibrated by setting a number of pixels to an already-known distance within the photographic image.

Scanning vibrating electrode technique (SVET)

SVET was used to study the localised corrosion characteristics and the relative corrosion performance. It is a powerful technique in corrosion research and has been employed in a range of investigations, such as galvanic corrosion, pitting corrosion, corrosion inhibitors, stress corrosion cracking, and cut-edge corrosion[4,16,17,21,22,34–37]. For surface corrosion SVET experiments, a square area of 36 mm^2 (6 mm × 6 mm) masked off using 3 M non-conductive polytetrafluoroethylene (PTFE) tape was exposed to the electrolyte. 29 measurements were made along both the width and length of the exposed area generating 841 data points for each scan. For cut-edge SVET corrosion experiments, samples were hot-mounted cross-sectionally in a non-conductive resin, ground using silicon carbide (SiC) paper to a European P grade P4000 grit finish and polished with aqueous 1 µm diamond suspension. A rectangular area of 30 mm^2 (10 mm×3 mm) was masked off using 3 M non-conductive PTFE tape and was exposed to the electrolyte. 34 measurements on the x-axis and 50 measurements on the y-axis were made of the exposed area generating 1700 data points for each scan. A schematic diagram of SVET samples used for investigations is shown in Fig. 16. Scans were taken every hour for 24 h and three tests were carried out for each material. The dissolved oxygen concentration in the bulk electrolyte was presumed to be equal to the equilibrium concentration value for air-saturated water i.e. 2.8×10^{-4} $mol.dm^{-3}$ [17].

The SVET consist of a glass-encased 125 µm platinum microtip vibrating perpendicularly at a height of 100 µm from the corroding surface at a constant frequency of 140 Hz with an amplitude of 25 µm. The SVET detects the alternating potential associated with ionic current fluxes due to oxidation and reduction reactions, therefore, enabling monitoring of the temporal and spatial behaviour of local anodes and cathodes on the material. The potential gradient is directly proportional to ionic current flux in the direction of vibration. The techniques detail instrumentation, operating and calibration procedures have been explained in detail elsewhere[34,38–41]. In addition to mechanistic information, SVET enables semi-quantitative measurement of metal loss through the integration of anodic current densities per scan with subsequent application of Faraday's law. Since various assumptions are made in these calculations the determined mass loss is semi-quantitative but proves to be useful in comparing materials of similar composition. The mass loss calculations and limitations of the method are discussed in detail elsewhere[16,17,21,35].

Several estimations are made when calculating the SVET metal loss; it is assumed that the corrosion activity remains constant between the scans and Zn^{2+} (Zn ions) are released during the anodic activities. Metal loss is estimated by the integration of all measured positive currents followed by the application of Faraday's law. Measured potentials (V) are converted to the current density (Am^{-2}), j_z, by multiplying it with the calibration factor. The total anodic current (i) is obtained using Eq. 5.

$$i = \int_0^x \int_0^y j_z(x,y)\,dx\,dy \tag{5}$$

Where,

x = length of the scan area

y = breadth of the scan area

As corrosion activities are assumed to be constant between the hourly scans and multiplying the current (i) by time (t) (3600 s), charge (Q) is calculated as shown in below equation.

$$Q = i.t \tag{6}$$

The SVET metal loss is calculated by entering the value of Q and the other relevant information of the corroding material under investigation into the Faraday equation as shown in below equation.

$$Metal\ loss(m) = \frac{Q}{n.F} A_r \tag{7}$$

Where,

Q = charge

F = Faraday's constant (96,487 $C.mol^{-1}$)

N = number of electrons (2 for Zinc)

A_r =atomic weight (65 g for Zinc)

The total metal loss can be calculated by summating the total number of scans.

Electrochemical measurements

OCP and LPR measurements were performed using Gamry Interface 1010E potentiostat. A platinum-plated electrode and saturated calomel electrode (SCE) were used as a counter and reference electrode respectively to create a 3-electrode set-up. The samples were rinsed using deionised water and ethanol and an area of 0.78 cm^2 was exposed to the electrolyte. All experiments were carried out in 0.17 M NaCl over 24 h. During LPR measurements, samples were polarised by ±15 mV from open circuit potential (OCP) at a scan rate of 0.166 mVs^{-1}. OCP measurements were followed immediately by LPR on the same sample so that the thermodynamics and

kinetics could be ascertained from a consistently exposed surface. OCP was measured for 300 s followed by a LPR measurement. Although during the LPR measurement, the sample surface was polarised ±15 mV from OCP, the sample surface was allowed to stabilise before the next OCP measurement was taken. Measurements were taken every hour for 24 h and two tests were carried out for each material.

Time-lapse microscopy (TLM)

TLM is an effective technique that facilitates capturing images of corroding surfaces at a microstructural level under immersion conditions and has been used to investigate localised corrosion[16,18,21] and inhibitors' efficiency[17,35] on Zn alloys. The TLM detailed methodology has been described elsewhere[17]. The samples were prepared as mentioned in section 5.2.1. A circular area of 0.785 mm^2 was masked off using PTFE tape and was exposed to the electrolyte. A digital camera (Infinity 2) connected to the Meiji Techno 7100 optical microscope was used to obtain images under immersion conditions. An image was taken every two minutes and compiled into a time-lapse video using Microsoft Movie Maker.

Data availability

The raw/processed data required to reproduce these findings cannot be shared at this time as the data also forms part of an ongoing study.

Received: 27 April 2024; Accepted: 7 July 2024;
Published online: 29 July 2024

References

1. Marder, A. R. The metallurgy of zinc-coated steel. *Prog. Mater. Sci.* **45**, 191–271 (2000).
2. Perkins, J. & Bornholdt, R. A. The corrosion product morphology found on sacrificial zinc anodes. *Corros. Sci.* **17**, 377–384 (1977).
3. Marder, A. R. & Goodwin, F. E. *The Metallurgy of Zinc Coated Steels*. *The Metallurgy of Zinc Coated Steels* https://doi.org/10.1016/C2020-0-04502-0 (2023).
4. Elvins, J., Spittle, J. A. & Worsley, D. A. Microstructural changes in zinc aluminium alloy galvanising as a function of processing parameters and their influence on corrosion. *Corros. Sci.* **47**, 2740–2759 (2005).
5. Raja, V. S., Panday, C. K., Saji, V. S., Vagge, S. T. & Narasimhan, K. An electrochemical study on deformed galvanneal steel sheets. *Surf. Coatings Technol*. https://doi.org/10.1016/j.surfcoat.2006.03.044 (2006).
6. Dan, A., Bijalwan, P. K., Pathak, A. S. & Bhagat, A. N. A review on physical vapor deposition-based metallic coatings on steel as an alternative to conventional galvanized coatings. *J. Coat. Technol. Res.* **19**, 403–438 (2022).
7. Shih, H., Hsu, J., Sun, C. & Chung, S. The lifetime assessment of hot-dip 5% Al–Zn coatings in chloride environments. *Surf. Coat. Technol.* **150**, 70–75 (2002).
8. Watkins, K. G., Jones, R. D. & Beahan, P. G. Electrochemical investigation of the corrosion rate of 55 aluminium-zinc alloy coated steel. *Mater. Lett.* **8**, 26–30 (1989).
9. Prosek, T., Persson, D., Stoulil, J. & Thierry, D. Composition of corrosion products formed on Zn–Mg, Zn–Al and Zn–Al–Mg coatings in model atmospheric conditions. *Corros. Sci.* **86**, 231–238 (2014).
10. Salgueiro Azevedo, M., Allély, C., Ogle, K. & Volovitch, P. Corrosion mechanisms of Zn(Mg,Al) coated steel: 2. The effect of Mg and Al alloying on the formation and properties of corrosion products in different electrolytes. *Corros. Sci.* **90**, 482–490 (2015).
11. Schuerz, S. et al. Corrosion behaviour of Zn – Al – Mg coated steel sheet in sodium chloride-containing environment. *Corros. Sci.* **51**, 2355–2363 (2009).
12. Thierry, D., Persson, D., Luckeneder, G. & Stellnberger, K.-H. Atmospheric corrosion of ZnAlMg coated steel during long term atmospheric weathering at different worldwide exposure sites. *Corros. Sci.* **148**, 338–354 (2019).
13. Volovitch, P., Vu, T. N., Allély, C., Abdel Aal, A. & Ogle, K. Understanding corrosion via corrosion product characterization: II. Role of alloying elements in improving the corrosion resistance of Zn–Al–Mg coatings on steel. *Corros. Sci.* **53**, 2437–2445 (2011).
14. Volovitch, P., Allely, C. & Ogle, K. Understanding corrosion via corrosion product characterization: I. Case study of the role of Mg alloying in Zn–Mg coating on steel. *Corros. Sci.* **51**, 1251–1262 (2009).
15. Duchoslav, J., Arndt, M., Keppert, T., Luckeneder, G. & Stifter, D. XPS investigation on the surface chemistry of corrosion products on ZnMgAl-coated steel. *Anal. Bioanal. Chem.* **405**, 7133–7144 (2013).
16. Wint, N. et al. The ability of Mg2Ge crystals to behave as 'smart release' inhibitors of the aqueous corrosion of Zn-Al-Mg alloys. *Corros. Sci.* **179**, 109091 (2021).
17. Sullivan, J. et al. In situ monitoring of corrosion mechanisms and phosphate inhibitor surface deposition during corrosion of zinc-magnesium-aluminium (ZMA) alloys using novel time-lapse microscopy. *Faraday Discuss*. https://doi.org/10.1039/c4fd00251b (2015).
18. Sullivan, J., Mehraban, S. & Elvins, J. In situ monitoring of the microstructural corrosion mechanisms of zinc–magnesium–aluminium alloys using time lapse microscopy. *Corros. Sci.* **53**, 2208–2215 (2011).
19. Prosek, T., Larché, N., Vlot, M., Goodwin, F. & Thierry, D. Corrosion performance of Zn–Al–Mg coatings in open and confined zones in conditions simulating automotive applications. *Mater. Corros.* **61**, 412–420 (2010).
20. Duchoslav, J. et al. Nanoscopic view on the initial stages of corrosion of hot dip galvanized Zn–Mg–Al coatings. *Corros. Sci.* **83**, 327–334 (2014).
21. Wint, N. et al. The effect of microstructural refinement on the localized corrosion of model Zn-Al-Mg alloy coatings on steel. *J. Electrochem. Soc.* **166**, C3147–C3158 (2019).
22. Penney, D. J., Sullivan, J. H. & Worsley, D. A. Investigation into the effects of metallic coating thickness on the corrosion properties of Zn–Al alloy galvanising coatings. *Corros. Sci.* **49**, 1321–1339 (2007).
23. Xu, M. et al. Effects of cooling rate on the microstructure and properties of hot-dipped Zn–Al–Mg coatings. *Surf. Coat. Technol.* **444**, 128665 (2022).
24. Wint, N., Eaves, D., Williams, G. & McMurray, H. N. The effect of composition and thickness on the mechanism and kinetics of filiform corrosion occurring on zinc-aluminium-magnesium coated steel. *Corros. Sci.* **179**, 109168 (2021).
25. Tait, W. S. Electrochemical Corrosion Basics. In *Handbook of Environmental Degradation of Materials* 97–115 (Elsevier, 2018). https://doi.org/10.1016/B978-0-323-52472-8.00005-8.
26. Hinterberger, F., Maschek, W. & Faderl, J. Influence of typical process parameters on the microstructure of galfan coatings. in *Zinc-Based Steel Coating Systems: Production and Performance, Proceedings of an International Symposium, 1998 TMS Annual Meeting* 281–292 (1998).
27. Elsaadawy, E. A. et al. Coating weight model for the continuous hot-dip galvanizing process. *Metall. Mater. Trans. B* **38**, 413–424 (2007).
28. Miyata, Y. & Asakura, S. Oxygen reduction reaction at rust free iron surface in neutral unbuffered chloride solutions. *Corros. Sci.* **44**, 589–602 (2002).
29. Tada, E., Sugawara, K. & Kaneko, H. Distribution of pH during galvanic corrosion of a Zn/steel couple. *Electrochim. Acta* https://doi.org/10.1016/j.electacta.2003.10.012 (2004).
30. Tada, E., Satoh, S. & Kaneko, H. The spatial distribution of Zn2+ during galvanic corrosion of a Zn/steel couple. *Electrochim. Acta* https://doi.org/10.1016/j.electacta.2004.01.008 (2004).
31. Han, J. & Ogle, K. Editors' choice—dealloying of MgZn 2 intermetallic in slightly alkaline chloride electrolyte and its significance in corrosion resistance. *J. Electrochem. Soc.* **164**, C952–C961 (2017).

32. Ramgopal, T., Schmutz, P. & Frankel, G. S. Electrochemical behavior of thin film analogs of Mg(Zn, Cu, Al)[sub 2]. *J. Electrochem. Soc.* **148**, B348 (2001).
33. Dafydd, H., Worsley, D. A. & McMurray, H. N. The kinetics and mechanism of cathodic oxygen reduction on zinc and zinc-aluminium alloy galvanized coatings. *Corros. Sci*. https://doi.org/10.1016/j.corsci.2005.05.036 (2005).
34. Bastos, A. C., Quevedo, M. C., Karavai, O. V. & Ferreira, M. G. S. Review—on the application of the scanning vibrating electrode technique (SVET) to corrosion research. *J. Electrochem. Soc.* **164**, C973–C990 (2017).
35. Malla, A. D., Sullivan, J. H., Penney, D. J., Dunlop, T. & Barker, P. Mechanistic study on the corrosion behaviour of Zinc and Zinc-Calcium alloys designed for enhanced metallic coatings in the presence of chloride and phosphate ions. *Corros. Sci.* **213**, 110956 (2023).
36. Sheikholeslami, S. et al. Cut-edge corrosion behavior assessment of newly developed environmental-friendly coating systems using the Scanning Vibrating Electrode Technique (SVET). *Corros. Sci.* **192**, 109813 (2021).
37. Worsley, D. A., McMurray, H. N., Sullivan, J. H. & Williams, I. P. Quantitative assessment of localized corrosion occurring on galvanized steel samples using the scanning vibrating electrode technique. *Corrosion* **60**, 437–447 (2004).
38. Williams, G. & Neil McMurray, H. Localized corrosion of magnesium in chloride-containing electrolyte studied by a scanning vibrating electrode technique. *J. Electrochem. Soc.* **155**, C340 (2008).
39. Böhm, S., McMurray, H., Powell, S. & Worsley, D. Photoelectrochemical investigation of corrosion using scanning electrochemical techniques. *Electrochim. Acta* **45**, 2165–2174 (2000).
40. McMurray, H. N., Powell, S. M. & Worsley, D. A. Mechanistic changes in cut edge corrosion induced by variation of inhibitor pigmentation in organically coated galvanised steel. *Br. Corros. J.* **36**, 42–48 (2001).
41. Isaacs, H. S. The effect of height on the current distribution measured with a vibrating electrode probe. *J. Electrochem. Soc*. https://doi.org/10.1149/1.2085665 (1991).

Acknowledgements

We would like to thank the Galvanized Autobody Partnership programme for funding and its associated members for their valuable input. The authors would also like to thank Tata Steel UK for providing samples.

Author contributions

A.D.M.: Investigation, Methodology, Data curation, Formal analysis, Writing—original draft, Writing—review & editing, Validation. J.H.S.: Conceptualization, Methodology, Validation, Formal analysis, Supervision, Writing—original draft, Writing—review & editing, Funding acquisition, Resources. D.J.P.: Conceptualization, Methodology, Validation, Formal analysis, Supervision, Writing—original draft, Writing—review & editing, Funding acquisition, Resources. M.G.: Investigation, Data curation. D.B.: Investigation, Data curation. G.W.: Writing—review & editing, Validation, Supervision, Resources. F.G.: Writing—review, Resources. A.P.C.: Writing—review, Resources.

Competing interests

The authors declare no competing interests.

Additional information

Supplementary information The online version contains supplementary material available at https://doi.org/10.1038/s41529-024-00494-2.

Correspondence and requests for materials should be addressed to A. D. Malla.